Quantum noise properties of CT images with anatomical textured backgrounds across reconstruction algorithms: FBP and SAFIRE

Justin Solomon[a)]
Carl E. Ravin Advanced Imaging Laboratories, Department of Radiology, Duke University Medical Center, Durham, North Carolina 27705

Ehsan Samei
Carl E. Ravin Advanced Imaging Laboratories, Department of Radiology, Duke University Medical Center, Durham, North Carolina 27705 and Departments of Biomedical Engineering and Electrical and Computer Engineering, Pratt School of Engineering, Duke University, Durham, North Carolina 27705

Purpose: Quantum noise properties of CT images are generally assessed using simple geometric phantoms with uniform backgrounds. Such phantoms may be inadequate when assessing nonlinear reconstruction or postprocessing algorithms. The purpose of this study was to design anatomically informed textured phantoms and use the phantoms to assess quantum noise properties across two clinically available reconstruction algorithms, filtered back projection (FBP) and sinogram affirmed iterative reconstruction (SAFIRE).

Methods: Two phantoms were designed to represent lung and soft-tissue textures. The lung phantom included intricate vessel-like structures along with embedded nodules (spherical, lobulated, and spiculated). The soft tissue phantom was designed based on a three-dimensional clustered lumpy background with included low-contrast lesions (spherical and anthropomorphic). The phantoms were built using rapid prototyping (3D printing) technology and, along with a uniform phantom of similar size, were imaged on a Siemens SOMATOM Definition Flash CT scanner and reconstructed with FBP and SAFIRE. Fifty repeated acquisitions were acquired for each background type and noise was assessed by estimating pixel-value statistics, such as standard deviation (i.e., noise magnitude), autocorrelation, and noise power spectrum. Noise stationarity was also assessed by examining the spatial distribution of noise magnitude. The noise properties were compared across background types and between the two reconstruction algorithms.

Results: In FBP and SAFIRE images, noise was globally nonstationary for all phantoms. In FBP images of all phantoms, and in SAFIRE images of the uniform phantom, noise appeared to be locally stationary (within a reasonably small region of interest). Noise was locally nonstationary in SAFIRE images of the textured phantoms with edge pixels showing higher noise magnitude compared to pixels in more homogenous regions. For pixels in uniform regions, noise magnitude was reduced by an average of 60% in SAFIRE images compared to FBP. However, for edge pixels, noise magnitude ranged from 20% higher to 40% lower in SAFIRE images compared to FBP. SAFIRE images of the lung phantom exhibited distinct regions with varying noise texture (i.e., noise autocorrelation/power spectra).

Conclusions: Quantum noise properties observed in uniform phantoms may not be representative of those in actual patients for nonlinear reconstruction algorithms. Anatomical texture should be considered when evaluating the performance of CT systems that use such nonlinear algorithms. © *2014 American Association of Physicists in Medicine.* [http://dx.doi.org/10.1118/1.4893497]

1. INTRODUCTION

The recently published report from the Summit on Management of Radiation Dose in Computed Tomography (CT) delineated the steps required to achieve routine submillisievert doses in clinical CT.[1] One step listed in that report is the development of image quality metrics that are clinically relevant and can be used to safely optimize and guide the implementation of protocols that take advantage of emerging dose-reduction technologies. One such technology that has the potential to enable reduced patient doses and maintain

diagnostic image quality is iterative reconstruction (IR). The principal advantage of IR algorithms is that they allow detailed physics models to be incorporated into the reconstruction process and thus should improve image quality compared to the traditional filtered back projection (FBP) algorithms.[2] Although IR algorithms have existed since the inception of CT, they quickly became impractical for typical clinical workflows due to their high computational demands. Recently, the availability of higher computational power has allowed for clinical implementation of IR. Currently, IR algorithms are commercially available from all major CT vendors[2]

and are beginning to be incorporated into clinical protocols. Therefore, there is a clinical need to develop a methodology to assess image quality and the corresponding dose reduction potential of these commercially available IR algorithms. Because most IR algorithms are nonlinear in nature, the systematic determination of safe dose reduction levels is a challenging task.

Many papers have recently been published in both technical[3–8] and clinical[9–25] journals demonstrating either improved image quality at equal dose or comparable image quality at lower dose for several commercial IR algorithms. Although the specific figures of merit differed, all of these studies used either phantoms or clinical trials (i.e., patient images) or both as the basis of their assessment. Clinical trials are necessary to validate a new technique and to confirm that a new technology is safe for clinical implementation. However, due to ethical, logistical, and economical considerations, clinical trials are generally not feasible if the goal is to robustly assess and optimize a new technique in a systematic and scientifically rigorous manner. For example, the ideal clinical trial for optimizing an IR algorithm in abdominal imaging may consist of first recruiting a large cohort of patients with known subtle lesions. Next, each patient would be imaged multiple times at different dose levels and the images reconstructed with FBP and IR. Finally, an observer study would be performed to determine which doses resulted in comparable diagnostic performance between FBP and IR. This type of study is clearly not feasible due to ethical concerns of giving multiple exposures to patients and the major logistical challenge of recruiting a large cohort of patients with known subtle lesions.

The practical alternative is to use phantoms. The advantage of phantoms is that they have known features that serve as the ground truth and they can be imaged multiple times with various scan settings. Thus, phantoms allow for the measurement of image quality metrics that reflect the physical properties of the CT system over the breadth of operational settings available (e.g., tube current, tube potential, reconstruction settings, etc). These metrics could be used as the basis of guiding and optimizing clinical protocols. The disadvantage of most available phantoms is that they are usually geometrically simple and use uniform backgrounds. Even anthropomorphic phantoms are generally uniform within a given organ. Actual patient images are clearly not uniform and contain detailed anatomical features and textures. These background anatomical textures can influence image quality, both because the presence of anatomical texture affects observer performance,[26–28] and because the presence of anatomical texture can influence physical image properties such as resolution[29–31] and quantum noise.[32] This complex relationship between anatomical variability and image quality cannot be accounted for in phantom studies that rely on simple uniform phantoms and thus the clinical relevance of such studies is questionable.[33] Therefore, there is a need to develop anatomically informed textured phantoms in order to characterize the complex relationship between anatomical variability and image quality for IR algorithms.

The purpose of this study was to design and build such textured phantoms and to demonstrate their utility by assessing the quantum noise properties of two reconstruction algorithms: FBP and a commercially available IR algorithm from Siemens Healthcare called *s*inogram *af*firmed *i*terative *re*construction (SAFIRE).

2. MATERIALS AND METHODS

Two separate phantom sections were designed to represent lung and soft-tissue texture. Both sections were designed as supplemental modules to the recently proposed Mercury phantom platform.[7] The phantoms were first designed virtually and then fabricated using rapid prototyping (i.e., 3D printing). The proceeding sections describe (a) a brief overview of the 3D printing technology used, (b) the design of the lung phantom, (c) the design of the soft-tissue phantom, and (d) an experiment in which the textured phantoms were utilized to assess the quantum noise properties of FBP and SAFIRE images.

2.A. 3D printing

3D printing is a rapidly evolving technology that allows for the fabrication of complex three-dimensional and multimaterial objects. Analogous to how a traditional printer creates physical documents from virtual documents; a 3D printer creates physical objects based on virtual computer models. 3D printers usually work by depositing plastic resins layer upon layer onto a platform to build the desired 3D object. This technology is finding applications in various areas of medicine including surgical planning,[34] component manufacturing for x-ray imaging systems,[35] phantom production,[36,37] and even printing real biological tissues.[38]

A multimaterial printer (Objet Connex, Stratasys Ltd.) was used for this study. This printer is able to mix two base materials (plastic resins) in various proportions during the print in order to achieve an effective number of up to 14 materials in a single printed object. This functionality is desirable for designing CT phantoms because each printed material has unique x-ray attenuation properties. Thus it is possible to print phantoms with intricate textures and variations that mimic those of actual tissues. This printer can also accurately create objects within tolerances (20–85 μm) that are smaller than the typical resolution of a clinical CT system. This makes it possible to fabricate an intricate textured phantom with known ground truth with a tolerance that is appropriate for testing a CT system. To print a multimaterial 3D object on this system it is necessary to specify the geometry of each material via a polygon mesh file (e.g., a stereolithography file). The steps followed to create these mesh files for each phantom will be described with greater detail in the proceeding sections.

The materials for phantom construction were chosen according to the desired x-ray attenuation properties of the phantom. The x-ray attenuation properties of the printing materials were empirically measured. Small samples representing many of the available plastics were imaged at 80, 100, 120, and 140 kVp on a clinical CT system (Discovery 750HD, GE Healthcare). Regions of interest were drawn within the sample images to get mean Hounsfield unit (HU)
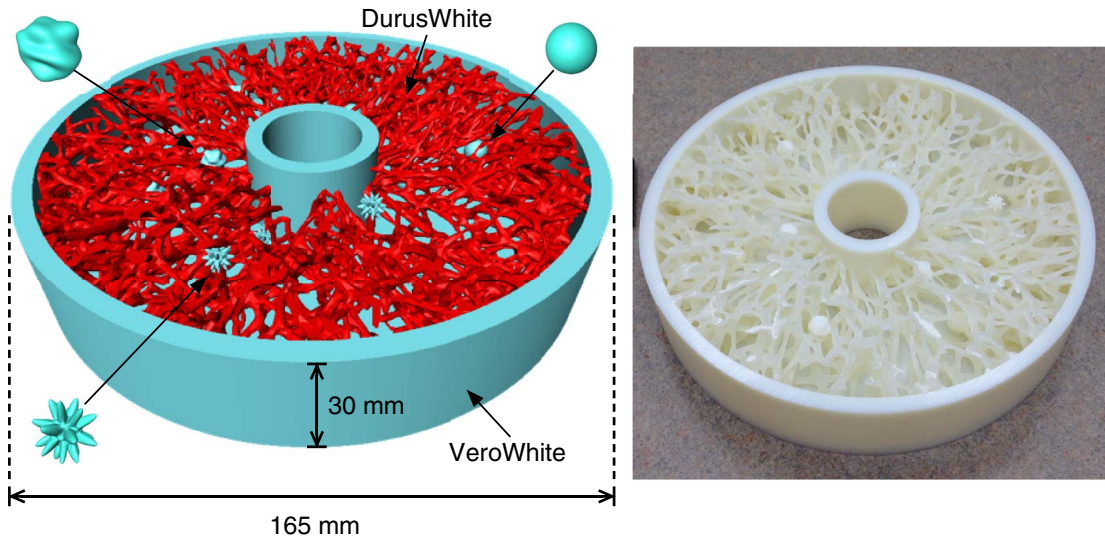
FIG. 1. A 3D rendering (left) of the lung phantom design. Each color in the rendering corresponds to a different material. The outer shell and lesions were printed with the VeroWhite material while the vessels were printed with DurusWhite. The image (right) shows the actual printed phantom. The attenuation properties of these materials can be found in Fig. 6.

values for each plastic type at each kVp. These HU measurements served as the basis of deciding which materials to use for fabricating the lung and soft-tissue phantoms.

2.B. Lung phantom

The lung texture section consisted of a cylindrical disk shell 165 mm in diameter and 30 mm in length with a 30 mm hole down the center (Fig. 1). The shell interior was designed to have an intricate network of vessel-like structures modeled using a recursive tree-growing algorithm developed for this project. The algorithm first placed starting seeds at random locations (uniformly distributed) on the inner shell wall. For each seed, a vessel tree was grown with six subdivisions. The algorithm created a binary tree by adding two new vessel branches at each endpoint. This process was repeated until the chosen number of subdivisions is achieved. Thus, a tree with n subdivisions had $2^{n+1} - 2$ vessel branches. The length and diameter of each new vessel branch were chosen randomly according to a uniform distribution between 13–18 and 2–2.5 mm for the length and diameter, respectively. The direction of each new segment was also chosen at random but was constrained to be within a $45°$ angle of the parent branch. The tree growing process, illustrated in Fig. 2, was implemented in MATLAB (vR2013a, Mathworks, Natick, MA).

The output of the tree-growing algorithm was a collection of tree data structures that specified the locations, directions, lengths, and diameters of every vessel branch. The data structures were used to create a polygon mesh representation of the vessel trees using a 3D graphics software package (MeVisLab, MeVis Medical Solutions, Brehmen, Germany). The tree-growing algorithm allowed for overlapping branches from different seed points. When the meshes were created, any overlapping vessels were merged, resulting in an additional node at the intersection point. The polygon meshes were then trimmed to fit within the phantom shell us-

ing 3D modeling software (Rhinoceros, McNeel North America, Seattle, WA). Further, 12 nodules (four spherical, four spiculated, and four lobulated) were virtually inserted into the phantom model. The shape of the lobulated nodules were based on earlier work in designing realistic virtual lesions.[39] Finally, the model was exported in mesh format (.stl) for 3D printing. Two materials were used, one for the outer shell and lesions (VeroWhite) and one for the vessels (DurusWhite).

2.C. Soft-tissue phantom

The soft-tissue texture section was designed as a solid disk volume with the same dimensions as the lung section (Fig. 3). Fatty soft-tissue texture was targeted for this section
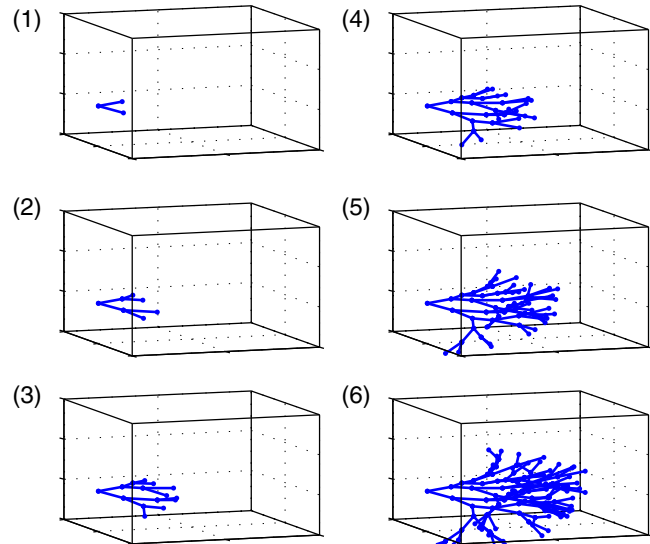

FIG. 2. Illustration of how the tree-growing algorithm generates a vessel tree from a seed point. Each frame shows a skeletonized representation of the tree after a given number of subdivisions.
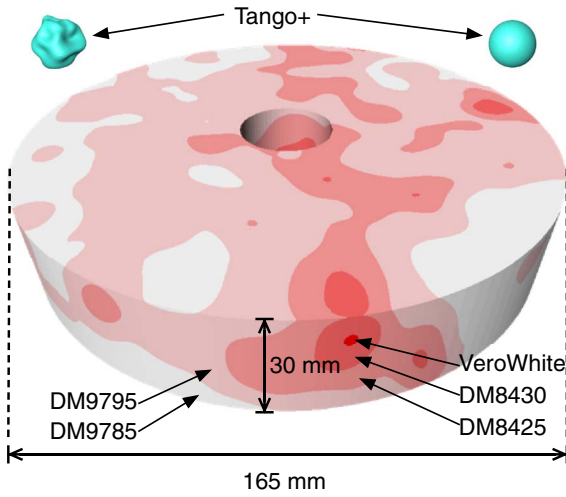
FIG. 3. A 3D rendering (left) of the soft-tissue phantom design. Each color in the rendering corresponds to a different material. The main body of the phantom was printed with the VeroWhite, DM8430, DM8425, DM9795, and DM9785 materials as indicated. The embedded lesions were printed with Tango-plus. The image (right) shows the actual printed phantom. The attenuation properties of these materials can be found in Fig. 6.

of the phantom based on "clustered lumpy backgrounds,"[40] a statistically defined image construct that has been used by perception scientists to model anatomical backgrounds.

For this study, a 3D clustered lumpy background image volume was synthesized (using a MATLAB script) as demonstrated in Fig. 4. The image volume was defined as the sum of a collection of anisotropic 3D exponential functions as

$$I(\vec{x}) = \sum_i \exp\left[-\alpha \frac{|\boldsymbol{R}_i(\vec{x} - \vec{c}_i)|^\beta}{\boldsymbol{R}_i \vec{L}}\right],   \quad (1)$$

where $\vec{x}$ denotes a 3D spatial coordinate (i.e., $\vec{x} = [x, y, z]$), $\vec{c}_i$ is the center of the ith exponential, $\boldsymbol{R}_i$ is the rotation matrix of the ith exponential, $\vec{L}$ is the characteristic length of the exponential in each direction (i.e., $\vec{L} = [L_x, L_y, L_z]$), and α and β are adjustable coefficients that affect the shape of the exponential as described by Bochud et $al.$[40] For this study, α was taken as 0.5, β was 2.0, and $\vec{L}$ was 20, 30, and 40 mm in the x, y, and z direction, respectively. Note that the use of the rotation matrix, $\boldsymbol{R}_i$, in Eq. (1) implies that the characteristic lengths, $\vec{L}$, correspond to the characteristic lengths in a transformed coordinate system. Thus each exponential function has a unique orientation. The locations and orientations of the exponential functions were randomly assigned as follows: First, a random number of seed points [Poisson distribution with mean of 500, Fig. 4(a)-large dots] were randomly placed (uniform distribution) throughout a 3D volume (165 × 165 × 30 mm box). Second, for each seed point, a random number of subpoints [Poisson distribution with mean of 10, Fig. 4(a)-small dots] were randomly placed (normal distribution) about each seed point. Each subpoint was randomly assigned an orientation vector (uniform distribution) that was then translated into a rotation matrix ($\boldsymbol{R}_i$). The final synthesized image volume [Fig. 4(b)] was taken as the sum over all exponential functions located at these subpoints using an isotropic voxel size of 1 mm. From this synthesized image volume, five mesh volumes [Fig. 4(c)] were created by
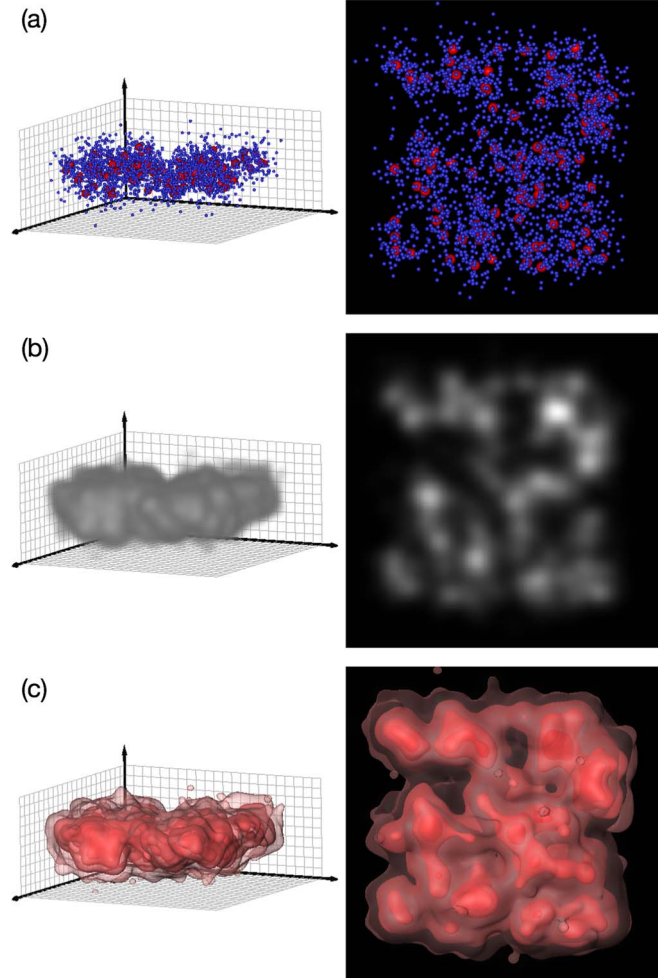

FIG. 4. An illustration showing how a clustered lumpy background in synthesized and used as the basis of mesh volumes, shown in 3D (left) and 2D (right). First the locations and orientations of each exponential function are randomly chosen (a). Next, the image volume is synthesized as the sum of overall exponential functions (b). Finally, the mesh volumes are created by calculating a series of concentric isosurfaces from the image volume (c).

calculating a series of concentric isosurfaces using MAT-LAB's *isosurface()* function. The mesh volumes were then trimmed to fit within the phantom dimensions using the Rhinoceros 3D modeling software package. Twelve low-contrast lesions (eight spherical and four anthropomorphic) similar to those in the lung texture phantom were incorporated into the model. The mesh volumes were then exported for 3D printing such that each volume was printed with a different material. A total of six materials were used to print this phantom section. Figure 3 shows the final design and materials used.

2.D. Quantum noise assessment

In order to demonstrate the utility of the textured phantoms, an experiment was designed to assess the noise properties of anatomically textured CT images reconstructed with FBP and IR. Both textured phantoms, along with a uniform phantom of similar size, were imaged in axial mode on a clinical multidetector row CT system (SOMATOM Definition Flash, Siemens Healthcare) operating at 120 kVp tube potential. All acquisitions were repeated 50 times and images were reconstructed with FBP and SAFIRE at 0.6 mm slice thickness using the B31s and I31s kernels, respectively. Note that hereafter SAFIRE will be referred to as the IR algorithm in text and figures. The reconstructed images, $I(\vec{x})$, can be characterized as the sum of a deterministic component, $\mu(\vec{x})$, and a zero-mean random noise component, $N(\vec{x})$, as

$$I(\vec{x}) = \mu(\vec{x}) + N(\vec{x}), \tag{2}$$

where $\vec{x}$ is a multidimensional spatial coordinate vector (i.e., $\vec{x} = [x, y]$). Noise magnitude, $\sigma(\vec{x})$, was defined as the standard deviation of $N(\vec{x})$ across the ensemble of repeated acquisitions (note that $STD[N(\vec{x})] = STD[I(\vec{x})]$). This definition allows for an assessment of noise magnitude on a voxel by voxel basis resulting in spatial maps of $\sigma(\vec{x})$. Further, by comparing $\sigma(\vec{x})$ between FBP and IR images, it is possible to compute noise reduction maps, $\sigma_{Red}(\vec{x})$, defined as the relative difference in noise magnitude between FBP and IR as

$$\sigma_{Red}(\vec{x}) = \frac{\sigma_{FBP}(\vec{x}) - \sigma_{IR}(\vec{x})}{\sigma_{FBP}(\vec{x})}. \tag{3}$$

The noise magnitude maps, $\sigma(\vec{x})$, were generated for each reconstruction algorithm and background type and were visually assessed to determine noise stationarity. These noise magnitude maps were then used to generate corresponding noise reduction maps, $\sigma_{Red}(\vec{x})$, for each background type. Also, histograms of $\sigma(\vec{x})$ and $\sigma_{Red}(\vec{x})$ were generated in order to assess the distribution of noise magnitude and noise reduction across background types.

The noise power spectrum (NPS) is defined as the Fourier transform of the autocorrelation of $N(\vec{x})$ and describes the spatial frequency content of the noise. This definition assumes that $N(\vec{x})$ is at least wide-sense stationary. A random process is considered wide-sense stationary if its first order statistics (e.g., mean and variance) are constant (i.e., spatially uniform), and if its second order statistics (e.g., autocorrelation) depend

only on the distance between voxels, as opposed to their absolute positions. In general, CT noise is actually nonstationary but is often assumed to be locally stationary within a small region of interest (ROI) in a uniform background. This assumption is generally valid for linear reconstruction algorithms (e.g., FBP) but may not be valid for nonlinear IR algorithms that can exhibit highly nonstationary noise when anatomical backgrounds are present.

Traditional methods to estimate the NPS involve directly taking the Fourier transform of a square ROI from a uniform region of the phantom (or from a subtracted image).[41] Due to the possibility of nonstationary noise, it was necessary to develop a new method to estimate NPS for arbitrarily shaped ROIs containing only pixels that have similar noise statistics. This method works by first estimating the noise autocorrelation, R_N, for a given arbitrarily shaped ROI, and then taking the Fourier transform of R_N. An algorithm to estimate R_N for an arbitrarily shaped ROI is given in the Appendix.

The NPS for a given ROI was calculated as

$$NPS(\vec{u}) = v_{\vec{x}} \cdot |\mathcal{F}[R_N(\Delta\vec{x})]|, \tag{4}$$

where $\vec{u}$ is a spatial frequency vector, $v_{\vec{x}}$ is the voxel (pixel) volume (area), $\Delta\vec{x}$ denotes the distance between two voxels, and $|\mathcal{F}[]|$ denotes the magnitude of the discrete Fourier Transform. Although this method allows for the NPS estimation of arbitrary dimension, in this study, only 2D NPS was considered (i.e., $\vec{x} = [x, y]$, $\vec{u} = [u, v]$, and $v_{\vec{x}}$ denotes the pixel area).

2D NPS was estimated for a single image slice in both FBP and IR across the three background types and averaged across the ensemble of 50 repeated acquisitions. For images that exhibited locally stationary noise, only a single NPS was estimated using a ring shaped ROI with an inner radius of 50 pixels and outer radius of 140 pixels, centered in the image field of view. For images that exhibited locally nonstationary noise, the ROI was further divided into two sub-ROIs corresponding to low and high noise regions. Further, radially averaged versions of the 2D spectra were generated using a standard radial binning technique.[41] The process to generate two NPS curves (low-noise and high-noise) for a single image with locally nonstationary noise is shown in Fig. 5.

3. RESULTS

The attenuation measurements for various materials are shown in Fig. 6. The measurements ranged from approximately 20 to 95 HU overall. For a given material, the HU values consistently increased as kVp increased by an average of approximately 30 HU between 80 and 140 kVp.

CT images and noise-only images of each phantom section are shown in Fig. 7 for each reconstruction algorithm. The noise magnitude maps and corresponding histograms are shown in Fig. 8. For FBP images, noise was globally nonstationary but locally stationary in all background types. For IR images, noise was both globally and locally nonstationary, especially in the lung phantom images. For FBP, the noise magnitude histograms demonstrated unimodal (i.e., single peaked) distributions of noise magnitude with mean
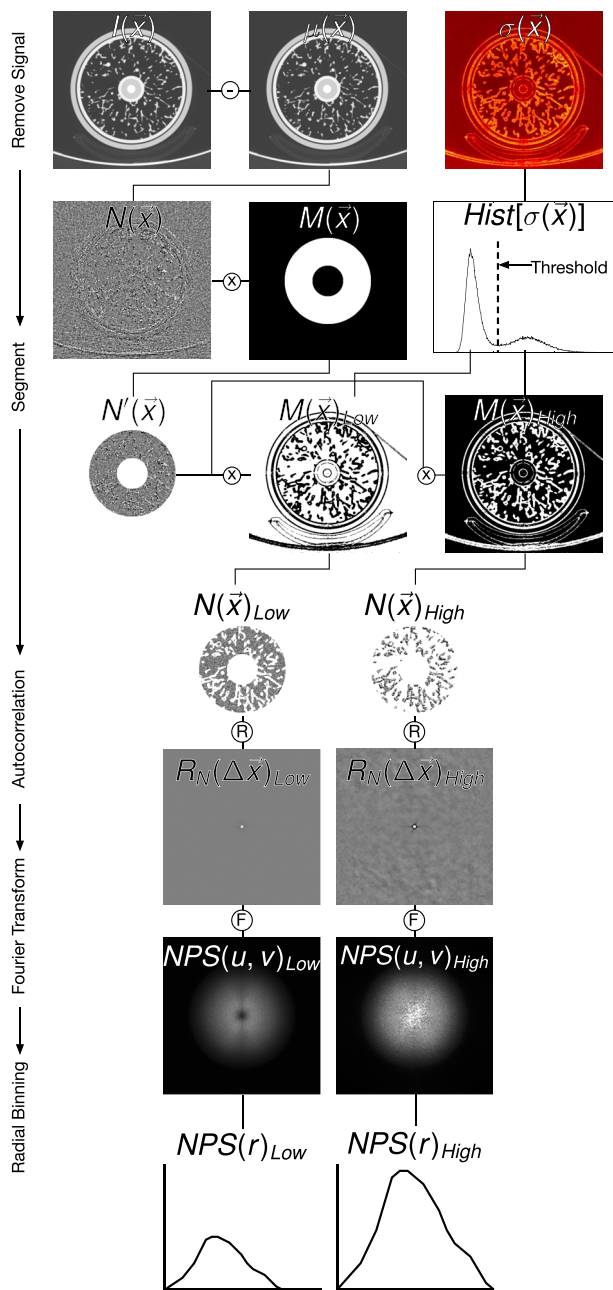
FIG. 5. An illustration showing the process of estimating low-noise and high-noise NPS curves for images with locally nonstationary noise. First, the deterministic signal was removed from the image, $I(\vec{x})$, by subtracting the ensemble mean image, $\mu(\vec{x})$, resulting in the zero mean noise image, $N(\vec{x})$. Next an ROI, $N'(\vec{x})$ was extracted by multiplying the noise image by a ring shaped binary mask, $M(\vec{x})$ (inner radius of 40 pixels and outer radius of 140 pixels). Concurrently, a histogram of the noise magnitude image, $\sigma(\vec{x})$, was generated. Based on this histogram, a threshold was used to segment the image into low and high noise regions. All pixels with noise less than the threshold were labeled as low noise and similarly, all pixels with noise greater than the threshold were labeled as high noise. This step ensures that the NPS was computed only within regions that have similar noise statistics, thus adhering to the assumption of noise stationarity within that region. The result of the segmentation was two binary masks corresponding to low and high noise regions, $M(\vec{x})_{Low}$ and $M(\vec{x})_{High}$, respectively. The masks were multiplied by the noise ROI, $N'(\vec{x})$, to achieve two sub-ROIs, $N(\vec{x})_{Low}$ and $N(\vec{x})_{High}$. Finally, the NPS for each sub-ROI was computed by estimating the autocorrelation (see the Appendix), taking the Fourier Transform, and then radially binning.
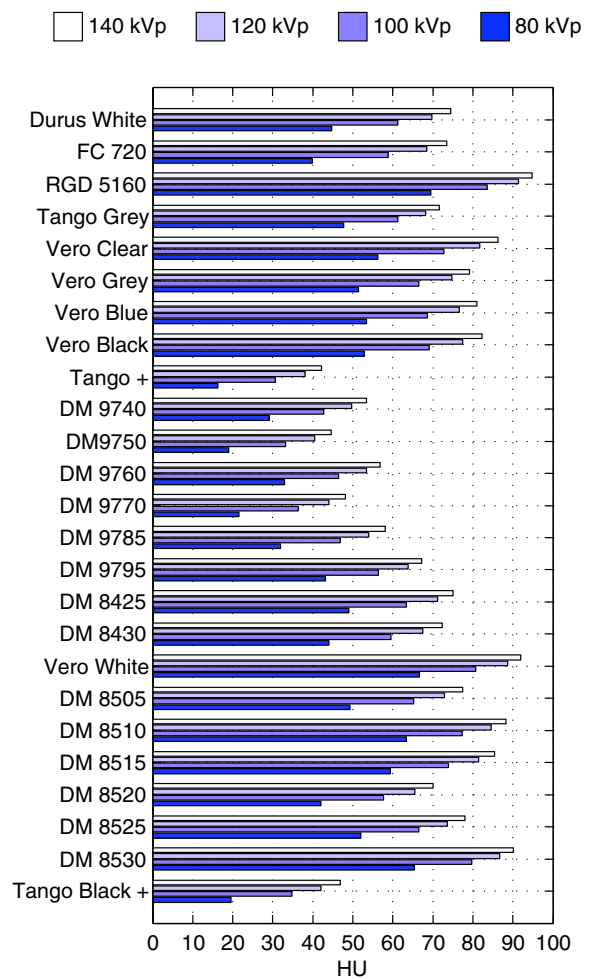

FIG. 6. Attenuation measurements of various materials used by the 3D printer for several kVp settings.

values of 18, 20, and 15 HU in the uniform, soft-tissue, and lung phantom, respectively. For IR, these distributions appeared bimodal with low (high) peaks corresponding to noise magnitude of 7 (16), 8 (15), and 6 (15) HU in the uniform, soft-tissue, and lung phantom, respectively. The noise reduction maps and corresponding histograms are shown in Fig. 9. These images demonstrate the spatial dependence on noise reduction and show how, in general, noise is reduced less for pixels near edges compared to pixels in uniform regions. For all background types, the majority of pixels showed a noise reduction of 60%, as demonstrated by the peaks in the noise reduction histograms. However, the textured phantoms had some pixels that did not benefit with as much noise reduction, again corresponding to the pixels on the edges.

The radially averaged NPS curves are shown in Fig. 10 for each background type and for FBP and IR images. Note that two NPS curves (denoted Lung-High and Lung-Low) were estimated from the lung IR images. This is because the lung IR images exhibited highly nonstationary noise that could be divided into two distinct ROIs corresponding to the two peaks of the noise magnitude histogram shown in Fig. 8. A noise threshold of 10 HU was used to segment high-noise from low-noise pixels (see Fig. 5). In general, the spectra from the
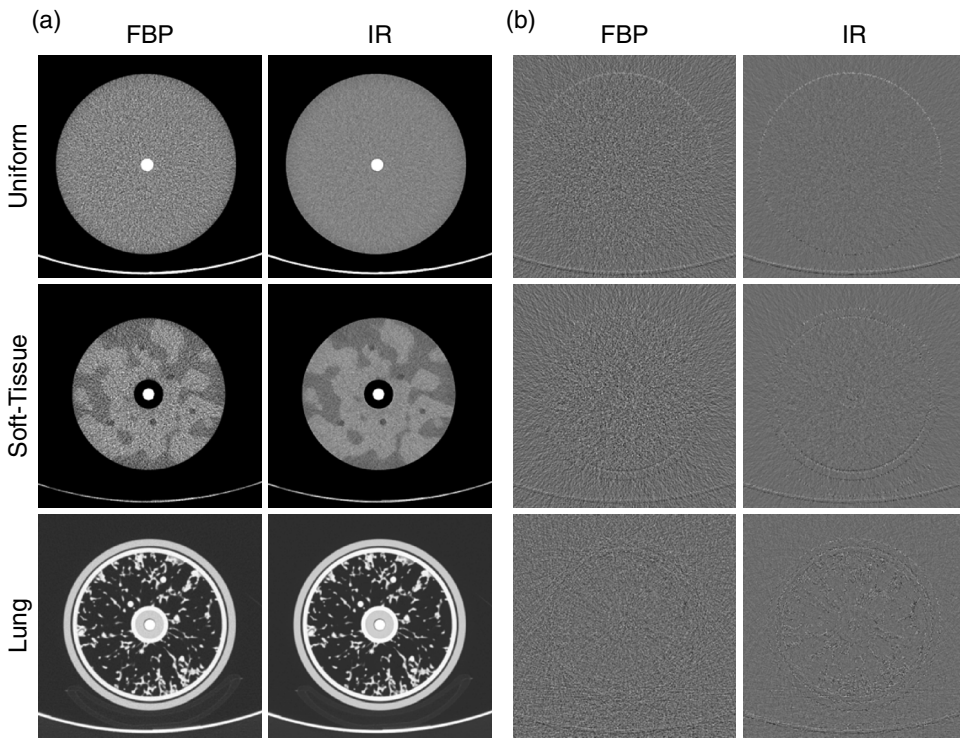
FIG. 7.   (a) CT images and (b) noise images of the uniform, soft-tissue, and lung phantoms for FBP and IR. The noise images represent one realization of $N(\tilde{x})$ and were found by subtracting the mean signal (averaged over the ensemble of repeated acquisitions).

IR images were shifted towards lower frequencies compared to FBP. However, the Lung-High spectrum did not appear as shifted as the other IR spectra.

4. DISCUSSION

We have demonstrated a technique to create anatomically informed textured phantoms for CT performance evaluation. By using 3D printing technology, we can create realistic inhomogeneous phantom volumes (Fig. 7) where the intricate details of the phantoms are known exactly. Further, we have demonstrated the utility of such phantoms by assessing the quantum noise properties of SAFIRE in the context of uniform and textured backgrounds. To our knowledge, no such phantoms are currently available and the quantum noise properties (in the presence of anatomical texture) of IR algorithms have not been previously reported.

IR algorithms control image noise via a regularization step that incorporates prior object information into the reconstruction.[2] Although the specific regularization schema varies greatly between different IR algorithms, the goal is always to reduce noise and preserve the fidelity of fine details. This paradigm necessitates a conservative approach to noise reduction for pixels near edges, and therefore, noise is not reduced as much near edges or structures. The results of this study are consistent with this principle, as evidenced by the noise magnitude maps and noise reduction maps of the lung phantom for IR (Figs. 8 and 9). Because the lung phantom contains many structures, the IR algorithm is not able to reduce noise magnitude consistently across the entire image. The result of this is a highly nonstationary noise in the IR

images. This demonstrates the need to consider anatomical textured backgrounds when assessing IR algorithms. Using simple uniform phantoms may produce misleading results with respect to the dose reduction potential of an IR algorithm.

The results of this study are also consistent with a recent report regarding the precision of nodule volume measurements in IR, where IR images exhibited nearly identical performance to that of FBP at the same dose.[42] This can be explained by the phenomenon characterized in this study. That is, the noise reduction of IR is severely reduced at edges, leaving performance (i.e., quantification of a nodule volume) comparable to FBP.

The results of the NPS analysis are also consistent with previous reports,[4] that is SAFIRE not only reduces noise magnitude but also affects the noise texture as is evidenced by the shift to lower frequencies for the IR spectra. However, a feature of SAFIRE that has not been previously reported is the fact that for highly textured images (such as the lung phantom images), the noise can have distinct regions of varying magnitude and texture. These distinct regions are visually perceivable in the noise images shown in Fig. 7 and their distinctiveness can be confirmed by examining the Lung-High and Lung-Low NPS curves in Fig. 10 (i.e., the Lung-High spectrum is not as shifted towards lower frequencies compared to the Lung-Low spectrum). Also, it is apparent from Fig. 10 that the IR Lung-High NPS curve is quite noisy at low frequencies. The lowest frequencies in the NPS correspond to correlations between pixels that are relatively far apart (i.e., for large lag distances in the noise autocorrelation). The shape of the ROI used to estimate the IR Lung-High autocorrelation function is
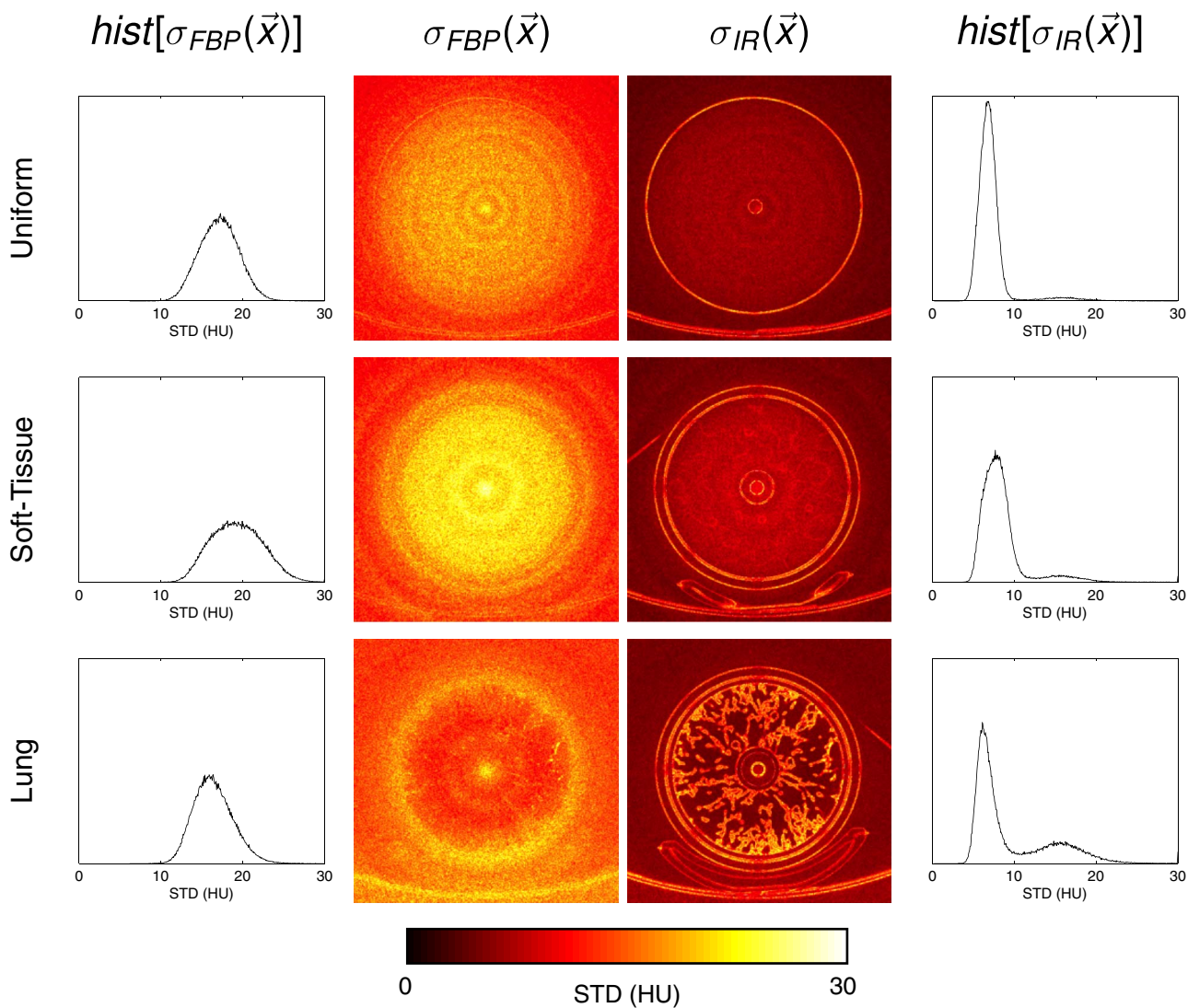
FIG. 8. Noise magnitude maps and corresponding noise magnitude histograms from a single CT slice for each background type and reconstruction algorithm. Noise magnitude was defined as the standard deviation of pixel values across the ensemble of 50 repeated acquisitions.

very irregular as it corresponds mostly to edge pixels around the vessel structures. Because of the irregular shape of this ROI, there are far fewer pixel pairs within the ROI at large distances from each other. This means that when estimating the autocorrelation at large lag distances, there are fewer pixel pairs over which to average. This results in a noisy autocorrelation function at large lag distances and thus a noisy NPS for low spatial frequencies.

The phantoms used in this study have approximately uniform attenuation across projection views as is evidenced by the relative uniformity of the noise magnitude maps for FBP (Fig. 8). It is likely that for phantom geometries that have nonuniform attenuation across projection views (e.g., oval shaped), the resulting reconstructed images would exhibit increased noise nonuniformity (i.e., nonstationarity). Also, in low-dose CT, electronic noise could result in increased noise nonuniformity. In such cases, care should be taken when applying the NPS analysis techniques to ensure that the noise is sufficiently stationary within the ROI. Similar to the IR images of the lung phantom, it may be necessary to divide

the image into multiple ROIs corresponding to varying noise levels within the image. Such measurements are highly facilitated by the ability to estimate the noise autocorrelation for an arbitrarily shaped ROI. Note that actual patient images have a much wider range of attenuating materials compared to these phantoms. In such images, there may be even larger noise variability across the image making it difficult to use only two noise classifications such as was done in this work (i.e., low noise and high noise). The relevance of the estimated autocorrelation/NPS may be compromised for such nonstationary images.

The experiment described in this paper represents only one of many possible uses of the textured phantoms. Future work will explore other analysis techniques aimed toward task-based performance evaluation. For example, it may be possible to assess spatial resolution and distortion by registering the phantom images with the mesh files used to create the phantom (i.e., compare the images with the ground truth). Also, the results in this study are based on axial scans and 2D analysis techniques that exclude any noise correlations in the
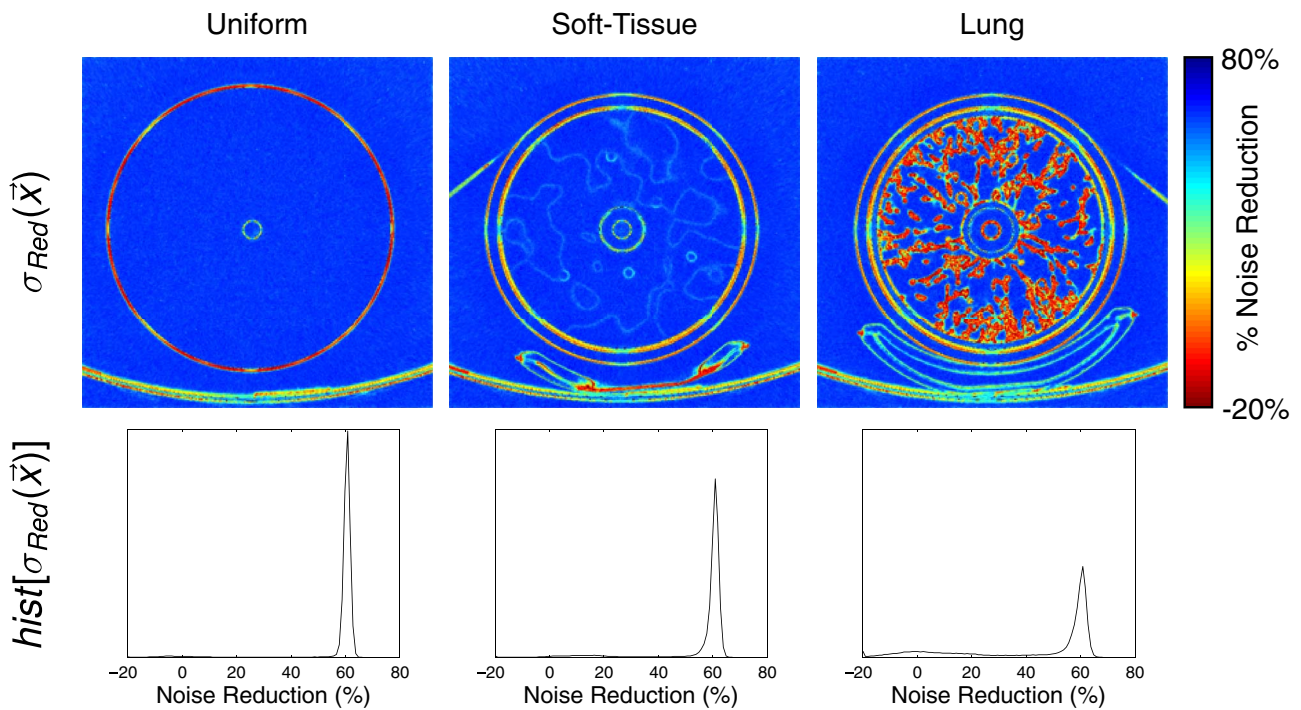
FIG. 9. Noise reduction maps and corresponding noise reduction histograms from a single CT slice for each background type. Noise reduction is defined as the relative difference of noise magnitude between FBP and IR.
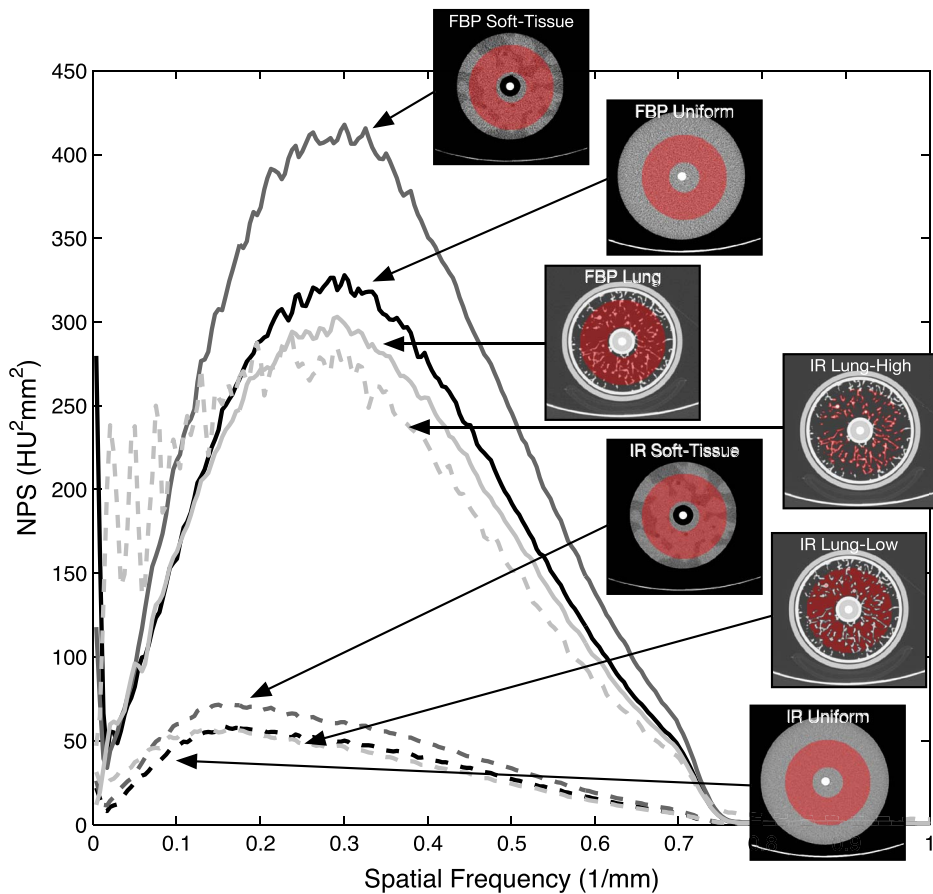

FIG. 10. NPS curves for all background types for FBP (solid lines) and IR (dotted lines). The shaded regions on the images represent the ROIs used to measure each NPS.

longitudinal direction. As the methods described in this paper are all extendable to 3D, future work will include helical scan modes and 3D analysis techniques. Finally, because the phantoms have embedded lesions, human or model observer studies could be designed.

Although the phantoms designed for this study represent an improvement over simple uniform phantoms, there is still the possibility of making them more realistic in future iterations. Several factors related to current 3D printing technology were limiting for this study. First, as can be seen in Fig. 6, the range of attenuation ($\sim$20–100 HU) that can be achieved from the available materials is not ideal as it would be desirable to mimic the range of attenuation seen in patient images (-1000–2000 HU). We are currently exploring methods (such as including iodinated resins) to achieve a wider range of attenuations in the printed phantoms. Second, preparing files for multimaterial printing is currently a cumbersome and time-consuming endeavor. This is a result of the need to create polygon meshes for each printed material. For solid multimaterial objects such as the soft-tissue phantom, it is necessary that all the mesh volumes be perfectly registered without any gaps, holes, or overlaps in order to avoid errors in the printing process. Achieving very fine details with many materials while avoiding gaps, holes, and overlaps in the meshes is not a trivial problem. For the purposes of making textured phantoms, it would be desirable to input voxelized phantom files as opposed to mesh files. It is hoped that these limitations will be obviated as 3D printing becomes more advanced.

5. CONCLUSIONS

It is possible to create realistic textured phantoms using 3D printing technology. The quantum noise properties of SAFIRE images were highly dependent on the background type (texture vs uniform). Therefore, background anatomical texture should be considered when evaluating the performance of CT systems, especially if the system uses iterative reconstruction.

ACKNOWLEDGMENTS

APPENDIX: AUTOCORRELATION ALGORITHM

Consider $N(x, y)$, a 2D zero-mean noise image. $N(x, y)$ could represent an entire CT image (with the signal removed) or a square ROI taken from the CT image. The noise autocorrelation, $R_N(x_1, y_1; x_2, y_2)$ is defined as the expected (i.e., average) correlation between pixels at locations (x_1, y_1) and (x_2, y_2) as

$$R_N(x_1, y_1; x_2, y_2) = E[N(x_1, y_1) \cdot N(x_2, y_2)], \quad \text{(A1)}$$

where $E[]$ is the expectation operator. By assuming that $N(x, y)$ is wide-sense stationary, the noise autocorrelation be-
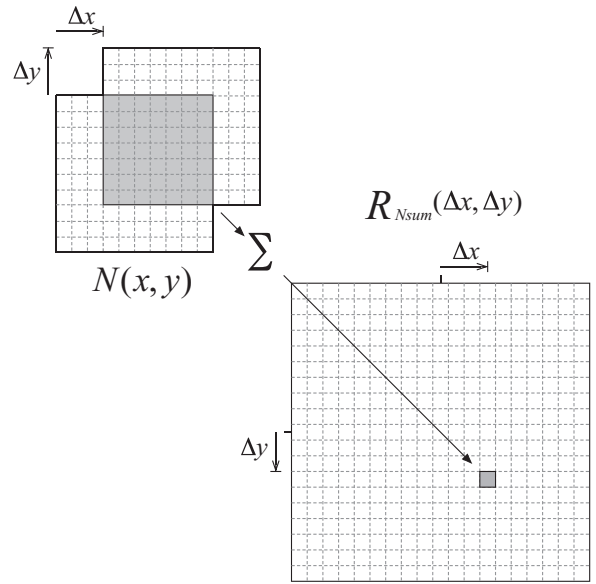

FIG. 11. Illustration showing how the sum autocorrelation, $R_{Nsum}(\Delta x, \Delta y)$, is calculated. A copy of the noise image, $N(x, y)$, is overlaid onto the original for a given lag ($\Delta x, \Delta y$). Overlapping (gray area) pixels are multiplied and the result is summed over all overlapping pixels. This sum represents one value in the autocorrelation. The process is repeated for all lag positions.

comes a function of only the *distance* between two voxels in the x and y directions (i.e., $R_N(x_1, y_1; x_2, y_2) \rightarrow R_N(\Delta x, \Delta y)$). Given $N(x, y)$, the autocorrelation is estimated by first computing the sum cross-correlation, $R_{Nsum}(\Delta x, \Delta y)$, between $N(x, y)$ and a copy of itself for all lag positions, Δx and Δy. This process is illustrated in Fig. 11. Mathematically, the sum correlation for a PxP image is given as

$$R_{Nsum}(\Delta x, \Delta y) = \sum_{x=0}^{P-1} \sum_{y=0}^{P-1} N(x, y) \\ \cdot N(x - \Delta x, y - \Delta y). \quad \text{(A2)}$$

Note that the size of the resulting sum correlation is 2P − 1. The final average correlation is computed by dividing the sum correlation by the number of pixels, $n(\Delta x, \Delta y)$, that contributed to $R_{Nsum}(\Delta x, \Delta y)$ as

$$R_N(\Delta x, \Delta y) = \frac{R_{Nsum}(\Delta x, \Delta y)}{n(\Delta x, \Delta y)}. \quad \text{(A3)}$$

Normally, if $N(x, y)$ is truly wide sense stationary, it would be desirable to use all available pixels to estimate R_N in order to minimize statistical uncertainty. In this case, $n(\Delta x, \Delta y)$ is given as the area of the overlapping region for a given lag position (see gray area in Fig. 11).

In certain cases, it is desirable to estimate the autocorrelation for an arbitrarily shaped ROI within $N(x, y)$ (Fig. 12). Let the ROI be defined by a binary mask image, $M(x, y)$ that has a value of 1 for pixels within the ROI and 0 for pixels not within the ROI. The first step is to multiply $N(x, y)$ by $M(x, y)$ (pixelwise) to get the masked image, $N'(x, y)$. This has the effect of setting all values outside of the ROI to 0. Next, the sum correlation, $R_{N'sum}(\Delta x, \Delta y)$ is computed for the masked image. In this way, the pixels that were not within
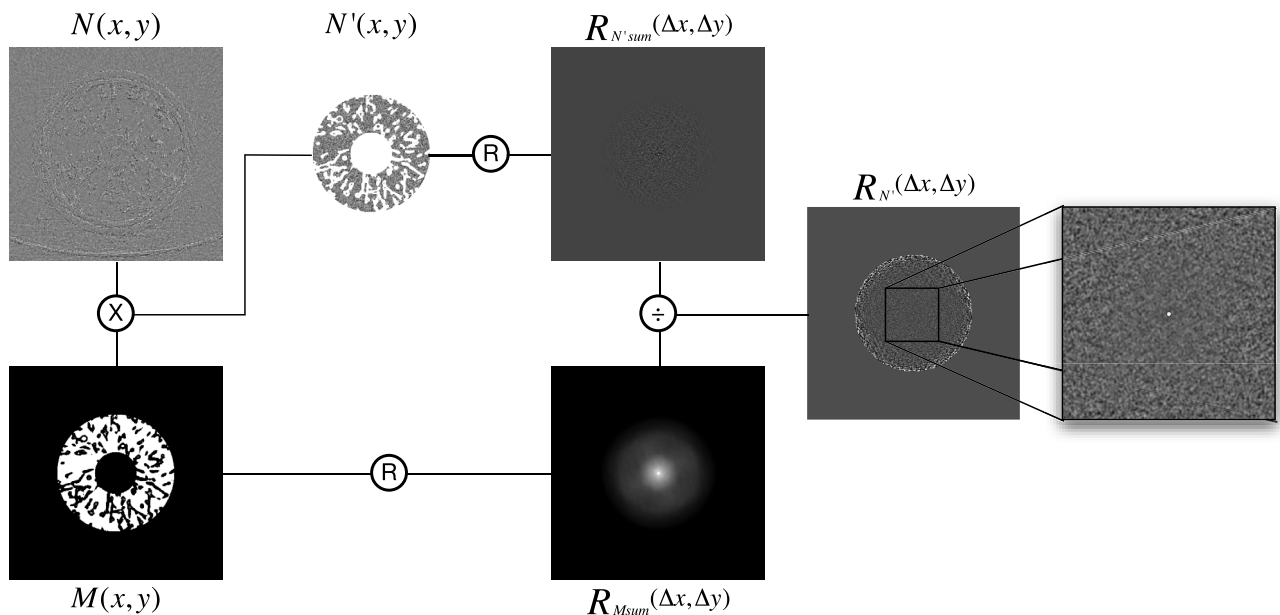
FIG. 12. Illustration of how the autocorrelation, $R_{N'}(\Delta x, \Delta y)$, is computed for an arbitrarily shaped ROI, $M(x, y)$ as described in the text. Note that X denotes pixelwise multiplication, $\div$ denotes pixelwise division, and R denotes the sum autocorrelation operation (see Fig. 11).

the ROI do not contribute to the sum. Next, it is necessary to compute the number of pixels that did contribute to the sum for each lag position, denoted $n'(\Delta x, \Delta y)$. This can be accomplished by computing the sum correlation of $M(x, y)$ as

$$n'(\Delta x, \Delta y)$$
$$= R_{Msum}(\Delta x, \Delta y)$$
$$= \sum_{x=0}^{P-1} \sum_{y=0}^{P-1} M(x, y) \Delta M(x - \Delta x, y - \Delta y). \quad \text{(A4)}$$

The final autocorrelation within the ROI, $R_{N'}$ is given by

$$R_{N'}(\Delta x, \Delta y) = \frac{R_{N'sum}(\Delta x, \Delta y)}{R_{Msum}(\Delta x, \Delta y)}. \quad \text{(A5)}$$

Note that depending on the size and shape of the ROI relative to the size of $N(x, y)$, it is possible that $n'(\Delta x, \Delta y)$ is zero for certain values of Δx and Δy. This results in a division by zero in Eq. (A5) and can be interpreted as not having any two pixels in the ROI at that given lag distance from each other. Generally this only happens for large Δx and Δy and when implementing this technique, it is necessary to crop the resulting autocorrelation function to the maximum lag distance at which $n'(\Delta x, \Delta y)$ is nonzero. In this study, the estimated autocorrelation functions were all cropped to represent a maximum lag distance of ± 128 pixels both the x and y directions. Also, in this paper, an ensemble of 50 noise realizations was acquired. The autocorrelation was estimated for each realization and the final autocorrelation was taken as the average across the ensemble.

a)Author to whom correspondence should be addressed. Electronic mail: justin.solomon@duke.edu

[1]C. H. McCollough, G. H. Chen, W. Kalender, S. Leng, E. Samei, K. Taguchi, G. Wang, L. Yu, and R. I. Pettigrew, "Achieving routine submillisievert CT scanning: Report from the summit on management of radiation dose in CT," Radiology 264, 567–580 (2012).

[2]M. Beister, D. Kolditz, and W. A. Kalender, "Iterative reconstruction methods in X-ray CT," Phys. Med. 28, 94–108 (2012).

[3]B. Chen, S. Richard, O. Christianson, X. Zhou, and E. Samei, "CT performance as a variable function of resolution, noise, and task property for iterative reconstructions," Proc. SPIE 8313, 83131K-1–83131K-6 (2012).

[4]C. Ghetti, F. Palleri, G. Serreli, O. Ortenzia, and L. Ruffini, "Physical characterization of a new CT iterative reconstruction method operating in sinogram space," J. Appl. Clin. Med. Phys. 14, 4347 (2013).

[5]W. A. Kalender, M. Beister, J. M. Boone, D. Kolditz, S. V. Vollmar, and M. C. Weigel, "High-resolution spiral CT of the breast at very low dose: Concept and feasibility considerations," Eur. Radiol. 22, 1–8 (2012).

[6]F. A. Mieville, F. Gudinchet, F. Brunelle, F. O. Bochud, and F. R. Verdun, "Iterative reconstruction methods in two different MDCT scanners: Physical metrics and 4-alternative forced-choice detectability experiments - A phantom approach," Phys. Med. 29(1), 99–110 (2012).

[7]J. M. Wilson, O. I. Christianson, S. Richard, and E. Samei, "A methodology for image quality evaluation of advanced CT systems," Med. Phys. 40, 031908 (9pp.) (2013).

[8]L. Yu, S. Leng, L. Chen, J. M. Kofler, R. E. Carter, and C. H. McCollough, "Prediction of human observer performance in a 2-alternative forced choice low-contrast detection task using channelized Hotelling observer: Impact of radiation dose and reconstruction algorithms," Med. Phys. 40, 041908 (9pp.) (2013).

[9]M. E. Baker, F. Dong, A. Primak, N. A. Obuchowski, D. Einstein, N. Gandhi, B. R. Herts, A. Purysko, E. Remer, and N. Vachani, "Contrast-to-noise ratio and low-contrast object resolution on full- and low-dose MDCT: SAFIRE versus filtered back projection in a low-contrast object phantom and in the liver," AJR, Am. J. Roentgenol. 199, 8–18 (2012).

[10]M. S. Bittencourt, B. Schmidt, M. Seltmann, G. Muschiol, D. Ropers, W. G. Daniel, and S. Achenbach, "Iterative reconstruction in image space (IRIS) in cardiac computed tomography: initial experience," Int. J. Cardiovasc Imaging 27, 1081–1087 (2011).

[11]W. Chang, J. M. Lee, K. Lee, J. H. Yoon, M. H. Yu, J. K. Han, and B. I. Choi, "Assessment of a model-based, iterative reconstruction algorithm (MBIR) regarding image quality and dose reduction in liver computed tomography," Invest. Radiol. 48, 598–606 (2013).

[12]J. G. Fletcher, K. L. Grant, J. L. Fidler, M. Shiung, L. Yu, J. Wang, B. Schmidt, T. Allmendinger, and C. H. McCollough, "Validation of dual-source single-tube reconstruction as a method to obtain half-dose images to evaluate radiation dose and noise reduction: phantom and human assessment using CT colonography and sinogram-affirmed iterative reconstruction (SAFIRE)," J. Comput. Assist. Tomogr. 36, 560–569 (2012).

[13]A. Gervaise, B. Osemont, S. Lecocq, A. Noel, E. Micard, J. Felblinger, and A. Blum, "CT image quality improvement using Adaptive Iterative Dose

Reduction with wide-volume acquisition on 320-detector CT," Eur. Radiol. **22**, 295–301 (2012).

[14]B. K. Han, K. L. Grant, R. Garberich, M. Sedlmair, J. Lindberg, and J. R. Lesser, "Assessment of an iterative reconstruction algorithm (SAFIRE) on image quality in pediatric cardiac CT datasets," J. Cardiovasc. Comput. Tomogr. **6**, 200–204 (2012).

[15]M. K. Kalra, M. Woisetschlager, N. Dahlstrom, S. Singh, M. Lindblom, G. Choy, P. Quick, B. Schmidt, M. Sedlmair, M. A. Blake, and A. Persson, "Radiation dose reduction with Sinogram Affirmed Iterative Reconstruction technique for abdominal computed tomography," J. Comput. Assist. Tomogr. **36**, 339–346 (2012).

[16]J. Leipsic, T. M. Labounty, B. Heilbron, J. K. Min, G. B. Mancini, F. Y. Lin, C. Taylor, A. Dunning, and J. P. Earls, "Estimated radiation dose reduction using adaptive statistical iterative reconstruction in coronary CT angiography: The ERASIR study," AJR, Am. J. Roentgenol. **195**, 655–660 (2010).

[17]J. Leipsic, T. M. Labounty, B. Heilbron, J. K. Min, G. B. Mancini, F. Y. Lin, C. Taylor, A. Dunning, and J. P. Earls, "Adaptive statistical iterative reconstruction: assessment of image noise and image quality in coronary CT angiography," AJR, Am. J. Roentgenol. **195**, 649–654 (2010).

[18]F. A. Mieville, L. Berteloot, A. Grandjean, P. Ayestaran, F. Gudinchet, S. Schmidt, F. Brunelle, F. O. Bochud, and F. R. Verdun, "Model-based iterative reconstruction in pediatric chest CT: Assessment of image quality in a prospective study of children with cystic fibrosis," Pediatr. Radiol. **43**(5), 558–567 (2012).

[19]F. A. Mieville, F. Gudinchet, E. Rizzo, P. Ou, F. Brunelle, F. O. Bochud, and F. R. Verdun, "Paediatric cardiac CT examinations: Impact of the iterative reconstruction method ASIR on image quality - preliminary findings," Pediatr. Radiol. **41**, 1154–1164 (2011).

[20]P. J. Pickhardt, M. G. Lubner, D. H. Kim, J. Tang, J. A. Ruma, A. M. del Rio, and G. H. Chen, "Abdominal CT with model-based iterative reconstruction (MBIR): Initial results of a prospective trial comparing ultralow-dose with standard-dose imaging," AJR, Am. J. Roentgenol. **199**, 1266–1274 (2012).

[21]F. Pontana, A. Duhamel, J. Pagniez, T. Flohr, J. B. Faivre, A. L. Hachulla, J. Remy, and M. Remy-Jardin, "Chest computed tomography using iterative reconstruction vs filtered back projection (Part 2): Image quality of low-dose CT examinations in 80 patients," Eur. Radiol. **21**, 636–643 (2011).

[22]F. Pontana, J. Pagniez, T. Flohr, J. B. Faivre, A. Duhamel, J. Remy, and M. Remy-Jardin, "Chest computed tomography using iterative reconstruction vs filtered back projection (Part 1): Evaluation of image noise reduction in 32 patients," Eur. Radiol. **21**, 627–635 (2011).

[23]C. Schabel, M. Fenchel, B. Schmidt, T. G. Flohr, C. Wuerslin, C. Thomas, A. Korn, I. Tsiflikas, C. D. Claussen, M. Heuschmid, and D. Ketelsen, "Clinical evaluation and potential radiation dose reduction of the novel sinogram-affirmed iterative reconstruction technique (SAFIRE) in abdominal computed tomography angiography," Acad. Radiol. **20**, 165–172 (2013).

[24]A. Winklehner, C. Karlo, G. Puippe, B. Schmidt, T. Flohr, R. Goetti, T. Pfammatter, T. Frauenfelder, and H. Alkadhi, "Raw data-based iterative reconstruction in body CTA: Evaluation of radiation dose saving potential," Eur. Radiol. **21**, 2521–2526 (2011).

[25]W. J. Yang, F. H. Yan, B. Liu, L. F. Pang, L. Hou, H. Zhang, Z. L. Pan, and K. M. Chen, "Can sinogram-affirmed iterative (SAFIRE) reconstruction improve imaging quality on low-dose lung CT screening compared with traditional filtered back projection (FBP) reconstruction?" J. Comput. Assist. Tomogr. **37**, 301–305 (2013).

[26]F. O. Bochud, J. F. Valley, F. R. Verdun, C. Hessler, and P. Schnyder, "Estimation of the noisy component of anatomical backgrounds," Med. Phys. **26**, 1365–1370 (1999).

[27]M. P. Eckstein, C. K. Abbey, and F. O. Bochud, "Visual signal detection in structured backgrounds. IV. Figures of merit for model performance in multiple-alternative forced-choice detection tasks with correlated responses," J. Opt. Soc. Am. A **17**, 206–217 (2000).

[28]W. Huda, K. M. Ogden, E. M. Scalzetti, D. R. Dance, and E. A. Bertrand, "How do lesion size and random noise affect detection performance in digital mammography?" Acad. Radiol. **13**, 1355–1366 (2006).

[29]J. A. Fessler and W. L. Rogers, "Spatial resolution properties of penalized-likelihood image reconstruction: Space-invariant tomographs," IEEE Trans. Image Process **5**, 1346–1358 (1996).

[30]S. Richard, D. B. Husarik, G. Yadava, S. N. Murphy, and E. Samei, "Towards task-based assessment of CT performance: System and object MTF across different reconstruction algorithms," Med. Phys. **39**, 4115–4122 (2012).

[31]J. W. Stayman and J. A. Fessler, "Regularization for uniform spatial resolution properties in penalized-likelihood image reconstruction," IEEE Trans. Med. Imaging **19**, 601–615 (2000).

[32]J. Solomon and E. Samei, "Are uniform phantoms sufficient to characterize the performance of iterative reconstruction in CT?," Proc. SPIE **8668**, 86684M (2013).

[33]D. J. Goodenough and K. E. Weaver, "Factors related to low contrast resolution in CT scanners," Comput. Radiol. **8**, 297–308 (1984).

[34]F. Rengier, A. Mehndiratta, H. von Tengg-Kobligk, C. M. Zechmann, R. Unterhinninghofen, H. U. Kauczor, and F. L. Giesel, "3D printing based on imaging data: Review of medical applications," Int. J. Comput. Assist. Radiol. Surg. **5**, 335–341 (2010).

[35]B. W. Miller, J. W. Moore, H. H. Barrett, T. Frye, S. Adler, J. Sery, and L. R. Furenlid, "3D printing in X-ray and Gamma-Ray Imaging: A novel method for fabricating high-density imaging apertures," Nucl. Instrum. Methods Phys. Res. A **659**, 262–268 (2011).

[36]N. Kiarashi, G. M. Sturgeon, L. W. Nolte, J. Y. Lo, J. T. Dobbins, W. P. Segars, and E. Samei, "Development of matched virtual and physical breast phantoms based on patient data," Proc. SPIE **8668**, 866805 (2013).

[37]T. T. Nguyen, H. N. Le, M. Vo, Z. Wang, L. Luu, and J. C. Ramella-Roman, "Three-dimensional phantoms for curvature correction in spatial frequency domain imaging," Biomed. Opt. Express **3**, 1200–1214 (2012).

[38]V. Mironov, T. Boland, T. Trusk, G. Forgacs, and R. R. Markwald, "Organ printing: Computer-aided jet-based 3D tissue engineering," Trends Biotechnol. **21**, 157–161 (2003).

[39]J. Solomon, R. Nelson, and E. Samei, "TU-C-103-01: A framework for 3D modeling of anthropomorphic lesions in CT," AAPM Annual Meeting, Indianapolis, IN (AAPM, College Park, MD, 2013), Vol. 40, p. 000436.

[40]F. Bochud, C. Abbey, and M. Eckstein, "Statistical texture synthesis of mammographic images with clustered lumpy backgrounds," Opt. Express **4**, 33–42 (1999).

[41]J. B. Solomon, O. Christianson, and E. Samei, "Quantitative comparison of noise texture across CT scanners from different manufacturers," Med. Phys. **39**, 6048–6055 (2012).

[42]B. Chen, H. Barnhart, S. Richard, M. Robins, J. Colsher, and E. Samei, "Volumetric quantification of lung nodules in CT with iterative reconstruction (ASiR and MBIR)," Med. Phys. **40**, 111902 (10pp.) (2013).